Journal of Catalysis 404 (2021) 607–619

Contents lists available at ScienceDirect

Journal of Catalysis

journal homepage: www.elsevier.com/locate/jcat

Identification and quantification of distinct active sites in Hf-Beta zeolites for transfer hydrogenation catalysis

Blake A. Johnson [1], John R. Di Iorio [1], Yuriy Román-Leshkov *

Department of Chemical Engineering, Massachusetts Institute of Technology, 77 Massachusetts Ave., Cambridge, MA 02139, USA

ARTICLE INFO

Article history:
Received 31 July 2021
Revised 2 October 2021
Accepted 18 October 2021
Available online 29 October 2021

Keywords:
Acetonitrile
Pyridine
MPVO
Integrated molar extinction coefficient
Lewis acid
Zeolite
Tin-Beta
Hafnium-Beta

ABSTRACT

Despite the significant progress made in characterizing different framework heteroatom sites that exist in Lewis acidic zeolites with probe molecule adsorption and spectroscopy, methods to reliably quantify site counts remain indefinite and have been primarily limited to Sn and Ti Lewis acid sites. Here, methods to quantify framework Lewis acidic Hf^{4+} sites in zeolite Beta (Hf-Beta) with two Lewis base titrants (pyridine, deuterated acetonitrile) were developed using infrared (IR) spectroscopy. Lewis acid site counts for Hf-Beta zeolites were validated by measuring integrated molar extinction coefficients (IMECs; ε, cm μmol^{-1}) on Sn-Beta zeolites using identical Lewis base titrants to benchmark site counts with established literature procedures to quantify Lewis acid sites in Beta zeolites from IR spectra. Highlighting the importance of benchmarking active site counts against well-established experimental protocols, IMECs of CD_3CN bound to open (ε(Sn; 2316 cm^{-1}): 1.80 ± 0.25) and closed (ε(Sn; 2308 cm^{-1}): 3.76 ± 0.33) Sn sites were ~ 1.8x larger than those previously reported while total Lewis acid site counts agreed with those measured by pyridine (ε(Sn; 1451 cm^{-1}): 1.58 ± 0.16) on six different Sn-Beta zeolites. IMECs measured for IR peaks reflecting pyridine bound to Lewis acidic Hf sites (ε(Hf; 1448 cm^{-1}): 1.54 ± 0.21) and CD_3CN bound to open (ε(Hf; 2313 cm^{-1}): 2.40 ± 0.22) and closed (ε(Hf; 2307 cm^{-1}): 3.55 ± 0.41) Hf sites, gave similar counts for the total number of Lewis acidic sites across six Hf-Beta zeolites (Si/Hf = 100–413). Consistent with previous reports with Sn-Beta catalysts where open Sn sites are responsible for catalytic turnover, apparent first and zero-order MPVO rate constants (0.01–1 M cyclohexanone in 2-butanol; per total Hf, 373 K) correlated with the total number of open Hf sites, per total Hf, but not with the total number of closed Hf sites or total Lewis acid site counts. Measured initial MPVO rates (0.1 M cyclohexanone in 2-butanol, per open Hf, 373 K) were ~ 25x higher on hydrophobic Hf-Beta-F than on hydrophilic Hf-Beta-OH zeolites. Overall, the apparent first-order MPVO rate constants (2-butanol solvent, per open Hf, 373 K) were ~ 6x higher on Hf-Beta-F than on Hf-Beta-OH zeolites. The characterization methods reported here enable normalization of MPVO turnover rates on Sn- and Hf-Beta zeolites by their number of open sites. This enables performing quantitative rate comparisons across Lewis acid zeolites of varying active site identity, solvation, and pore topology used in liquid-phase catalysis.

1. Introduction

The concept of a turnover frequency (TOF) provided the foundation for the rigorous comparison and reproduction of heterogeneous catalytic reaction data across different laboratories [1]. As part of his legacy, Prof. Michel Boudart instilled that catalytic reaction rates can only be accurately reproduced or compared across different catalysts if they are normalized to a proper measure of the number of catalytic active sites [2,3]. This led to the development of experimental techniques (e.g., CO chemisorption) to measure catalytic surface areas or the number of active sites [4–8], allowing us not only to quantitate kinetics, but also to identify structure-sensitive (or insensitive) reactions [1,9–14], quantitate support-induced effects [15–19], and readily identify heat and mass transfer artifacts in kinetic measurements [20,21]. Rigorous normalization of turnover rates becomes particularly important during liquid phase catalysis in microporous materials where rate measurements, compared across catalysts of varying topology, metal identity, and framework composition, are further complicated by the presence of a solvating intraporous fluid phase. Active centers in these materials comprise (i) primary sites that bind adsorbates, (ii) secondary environments that confine intermediates and transition states, and (iii) coadsorbed molecules, clusters, and

* Corresponding author.
E-mail address: yroman@mit.edu (Y. Román-Leshkov).
[1] These authors have contributed equally.

https://doi.org/10.1016/j.jcat.2021.10.026
0021-9517/

solvent networks that interact with species along the reaction coordinate [22]. Thus, quantitative methods must be able to decouple the effects of active site identity and solvation from the confining pore geometry or presence of occluded moieties on the observed reaction rate along the reaction coordinate.

The unique water-tolerance and synthetic versatility of siliceous zeolites containing Lewis acidic tetravalent heteroatoms (e.g. Sn^{4+}, Zr^{4+}, Hf^{4+}) makes them ideally suited to activate oxygenates in the liquid-phase. However, titrimetric efforts to count active sites in these materials are complicated because the Lewis acidic heteroatoms can be incorporated into the framework either as fully connected tetrahedra ("closed" site) or as 3-fold coordinated species where a hydroxyl ligand completes the tetrahedral site ("open" site) [23–25,23,26]. As a result, titrants that are spectroscopically sensitive to these unique site types have been used for identification and quantification. Early evidence of distinct Lewis acid sites in Sn-containing zeolites was first reported by Corma and co-workers, who observed two peaks corresponding to different Lewis acidic Sn sites in the infrared (IR) spectrum of Sn-Beta saturated with deuterated acetonitrile (CD_3CN; $\nu(C{\equiv}N)$: 2308 and 2316 cm^{-1}). Density functional theory (DFT) was used to assign these peaks to closed and open Sn sites, respectively, on the basis of CD_3CN vibrational frequency calculations performed on small stannosilicate cluster models [27]. The assignments of distinct Sn sites have been further supported by additional evidence utilizing adsorbed probe molecules (e.g., CD_3CN, CO, trimethylphosphine oxide [TMPO]) and a combination of spectroscopic (e.g., IR, NMR) and DFT studies [23,26,28–35]. This body of work was the basis for the subsequent development of quantitative methods to count different Lewis acid site types in Sn-Beta zeolites [32].

Distinct coordination environments similar to those reported for Sn sites are presumably also present in Hf-, Ti-, and Zr-zeolites. Although significant progress has been made in characterizing different framework heteroatom sites that exist in these metallosilicates using IR spectra of adsorbed probe molecules, methods to reliably quantify site counts remain uncertain and primarily limited to Ti Lewis acid sites [30,32,36]. Of particular interest is the identification and quantification of Lewis acid sites in Zr- and Hf-Beta zeolites, which feature remarkable catalytic performance in a wide range of chemistries in organic media [37–39]. For example, both Zr- and Hf-Beta zeolites catalyze Meerwein-Ponndorf-Verley (MPV) type reactions with higher reaction rates than other Lewis acid site types [37–42]. But, to our knowledge, active site counting and rate normalization remains limited to a total metal basis. Additionally, it is frequently postulated that many reactions involving carbonyl substrates proceed over "open" framework Hf and Zr sites as the relevant active sites [38,42–44], but such assessments are often qualitative in nature. Multiple spectroscopic features have been observed in ^{31}P magic-angle spinning (MAS) NMR spectra of TMPO adsorbed on Ti-, Zr-, and Hf-Beta [30], and in IR spectra of CO adsorbed on Zr-Beta [45,46]. Precise identification of multiple Lewis acid sites in Zr- and Hf-Beta zeolites using CD_3CN, however, has led to conflicting reports whether one or two Lewis acid site types are present in IR spectra of adsorbed CD_3CN on Zr [46,47] and Hf-Beta [38,42]. Partial ion-exchange of Hf-Beta zeolites with Na^+ was shown to decrease self-aldol condensation reaction rates, presumably due to interactions between Na^+ and the open metal site [29], which was confirmed by IR spectra of adsorbed CD_3CN that showed a coincident decrease in the intensity of the peak associated with CD_3CN bound to framework Hf sites with increasing Na^+ content [42]. More recently, the ratio of the number of open to closed metal sites has been extracted from IR spectra of CD_3CN adsorbed on Lewis acid sites in Zr- and Hf-Beta zeolites after deconvolution using two component peaks representative of open and closed sites, but without reporting quantitative integrated molar extinction coefficients for these sites [38,47].

Here, we report integrated molar extinction coefficients (IMECs) from IR spectra of adsorbed pyridine and CD_3CN on Hf-Beta zeolites that enable the determination of the total number of Lewis acid sites, as well as the number of open and closed sites in these zeolites. We demonstrate that both titrants estimate the same number of Lewis acidic Hf sites on eight distinct Hf-Beta zeolites prepared via direct crystallization or solvent-assisted grafting methods. These site counts are supported by measured Meerwein-Ponndorf-Verley-Oppenauer (MPVO) transfer hydrogenation first and zero-order rate constants that correlate with the total number of open Hf sites, consistent with observations made on Sn-Beta zeolites, and present quantitative evidence that open Hf sites are the active sites for MPVO reactions in Hf-Beta zeolites. These results provide further insight into the complex relationship between active site identity, framework polarity, and reaction solvent that comprise confined active site structures in zeolite catalysts used for conversion of oxygenates in the liquid-phase.

2. Methods

2.1. Synthesis of metallosilicates

All zeolite samples are labeled as M−Beta−Y(X) where M is the framework heteroatom (Si for pure SiO_2 Beta, Sn, Ti, Zr, or Hf), -Y denotes crystallization in fluoride media (-F) or solvent-assisted grafting (–OH), and X is the Si/M molar ratio in the crystalline product determined by elemental analysis.

Hydrophobic zeolites were synthesized in the presence of F^- anions following previously reported procedures [37,48–50] with a molar composition of 1 SiO_2/y MO_x/ 0.54 TEAOH/ 0.54 HF/7.25 H_2O where y is the desired molar ratio of a framework heteroatom (M) on a per SiO_2 basis. The metal precursors used were: tin(II) chloride dihydrate ($SnCl_2{\cdot}2H_2O$, MilliporeSigma, 99.99 wt%), hafnium(IV) chloride ($HfCl_4$, MilliporeSigma, 98 wt%), zirconium(IV) oxychloride octahydrate ($ZrOCl_2{\cdot}8H_2O$, MilliporeSigma, 98 wt%), and titanium(IV) isopropoxide ($Ti(C_3H_7O)_4$, MilliporeSigma, 99.999 wt%). In a typical synthesis, an aqueous solution of tetraethylammonium hydroxide (TEAOH; Sigma-Aldrich, 40 wt%) was added to a perfluoroalkoxyalkane (PFA, Savillex Corp.) jar containing tetraethyl orthosilicate (TEOS; MilliporeSigma, >99 wt%) and stirred under ambient conditions for 90 min. Deionized water (18.2 MΩ-cm) was added and the resulting mixture was cooled in an ice bath for 15 min. In a separate glass vial, the desired amount of metal precursor was fully dissolved in 2 cm^3 of ethanol (Koptec, 200 proof) and then added dropwise to the TEOS/TEAOH/H_2O mixture while stirring in an ice bath. The mixture was left uncovered under stirring at ambient conditions to evaporate ethanol and excess water until the target molar ratios were reached. Hydrofluoric acid (HF; MilliporeSigma, 48 wt%, 99.999% trace metals basis) was then added dropwise and the mixture was stirred with a PTFE spatula until a homogeneous paste was achieved. Finally, calcined Si-Beta-F (10 wt% SiO_2 basis) was stirred into the mixture and transferred to PTFE-lined stainless-steel autoclaves and heated to 413 K in a static oven for 20 days or until a fully crystalline product was formed (up to 40 days).

Al-Beta zeolites (Si/Al = 12.5, CP814E, Zeolyst) were dealuminated by adding the zeolite powder to concentrated nitric acid (HNO_3; 50 cm^3 per $g_{zeolite}^{-1}$, 70 wt%, MilliporeSigma) in a sealed PFA jar and heating to 353 K for 24 h under stirring. Solids were recovered via centrifugation, washed with deionized water until the pH between washes was constant, dried at 373 K overnight

under ambient air, and then heated to 853 K (1 K min^{-1}) under flowing dry air (100 cm^3 min^{-1} per gram material; −80 °F dew point, Airgas) for 10 h.

Hydrophilic zeolites were synthesized by the solvent-assisted grafting of vacancy defects in dealuminated Beta zeolites under anhydrous conditions [49,51]. Briefly, dealuminated Beta zeolites (residual Si/Al > 5000) were dehydrated overnight at 523 K under dynamic vacuum (<0.1 Torr), cooled to room temperature under vacuum, and then held under a dry N_2 purge. In a separate flask, dichloromethane (for Sn grafting; DCM, MilliporeSigma, 99.8 wt %) or acetonitrile (for Hf grafting; CH_3CN, MilliporeSigma, 99.9 wt %, HPLC grade) was dried over 3A molecular sieves (previously dehydrated at 523 K overnight under dynamic vacuum; MilliporeSigma) for > 24 h under dry N_2 purge (100 cm^3 solvent per gram of dealuminated Beta). Dry CH_3CN was used instead of DCM for the preparation of Hf-Beta-OH zeolites due to observed limited solubility of $HfCl_4$ in dry DCM, which led to the formation of larger quantities of extraframework HfO_x species (UV–Vis spectra in Figure S5 in the Supporting Information). ~ 25 cm^3 of the dried solvent was then transferred to a N_2 filled glovebox and the desired amount of Sn (1 M $SnCl_4$ in DCM, MilliporeSigma) or Hf ($HfCl_4$, MilliporeSigma, 99.99 wt%) precursor was dissolved. The remaining dried solvent and the metal precursor solution was added to the dehydrated dealuminated Beta zeolite via cannula transfer under stirring and then heated to 313 K for 8 h.

All zeolite solids were recovered via centrifugation, washed alternately with deionized water and acetone (99.5 wt%, BDH Chemicals), and dried overnight under stagnant air at 373 K. The dried powders were then heated to 853 K (1 K min^{-1}) in a muffle furnace under dry air (100 cm^3 min^{-1} per gram material) for 10 h.

Zeolite samples containing extraframework Sn and Hf oxide species were synthesized by incipient wetness impregnation of Si-Beta-F with a solution of either $SnCl_2{\cdot}2H_2O$ or $HfCl_4$ dissolved in ethanol such that the final Si/M molar ratio was 100. The impregnated solids were then dried overnight at 373 K under stagnant air, then heated to 853 K (1 K min^{-1}) under dry air (100 cm^3 min^{-1}) for 10 h.

2.2. Catalyst characterization

Crystal structures were determined from powder X-ray diffraction (XRD) patterns collected on a Bruker D8 diffractometer equipped with a Cu Kα radiation (0.15406 nm) source by scanning between 5° and 40° 2θ at a rate of 0.077° s^{-1} and are shown in Figures S1 and S2 of the Supporting Information.

Elemental analysis was performed using an Agilent 7900 inductively coupled plasma mass spectrometry (ICP-MS) instrument by dissolving ~ 10 mg of zeolite powder in 200 μL of HF acid for 6 h then diluting with 2 wt% HNO_3 (Veritas Double Distilled, GFS Chemicals Inc.). Calibration curves prepared from standard solutions of 1000 ppm Al in 2% HNO_3 (TraceCERT, MilliporeSigma), 1000 ppm Hf in 5% HNO_3 and 0.5% HF (TraceCERT, MilliporeSigma), 1000 ppm of Sn in 10% HCl (TraceCERT, Sigma-Aldrich), 1000 ppm Ti in 2% HNO_3 (TraceCERT, MilliporeSigma), and 1000 ppm Zr in 2% HNO_3 and 0.2% HF (TraceCERT, MilliporeSigma) diluted in 2 wt% HNO_3.

Diffuse reflectance UV–Vis spectra were measured on a Cary 5000 spectrometer (Agilent) equipped with a DiffusIR diffuse reflectance accessory and environmental chamber (PIKE Technologies). UV–Vis spectra were collected on zeolite samples at 298 K after dehydration at 523 K (10 K min^{-1}) under flowing dry air for 2 h and measured relative to a barium sulfate ($BaSO_4$; 99 wt%, MilliporeSigma) background. Diffuse reflectance measurements were converted to absorbance using the Kubelka-Munk function and are shown in Figures S3-S5 of the Supporting Information.

2.3. Measurement of IR spectra

IR spectra were measured on a Bruker Vertex 70 spectrometer equipped with a liquid N_2 cooled Hg-Cd-Te (MCT) detector by averaging 128 scans at 4 cm^{-1} resolution and an aperture setting of 4 mm between 4000 and 400 cm^{-1}. All IR spectra were collected relative to an empty cell spectrum measured at 303 K under dynamic vacuum (<10^{-5} Torr, Edwards T-Station 75 Turbopump) after heating the empty cell to 673 K for 2 h under vacuum. Zeolite powders (~15 mg) were pressed into 13 mm diameter wafers, placed in a stainless steel sample holder (Harrick Scientific Products Inc.), and loaded into a high-temperature transmission IR cell (Harrick Scientific Products Inc.) sealed with KBr windows (32 × 3 mm; Harrick Scientific Products Inc.). The spectrometer and the space between the cell and the detector were continuously purged with dry N_2 (liquid N_2 boil-off and passed through activated 3A molecular sieves) to remove background traces of CO_2 and H_2O. Each sample was heated to 673 K (5 K min^{-1}) under flowing dry air (50 cm^3 min^{-1}) for 2 h, cooled under flowing air to 303 K (for CD_3CN and 2-butanol) or 423 K (for pyridine), and then evacuated until the pressure was steady at < 10^{-5} Torr. All dosing experiments were performed using the same Schlenk line manifold described previously [49]. Acetonitrile d_3 (CD_3CN; anhydrous, ≥99.8 atom% D, MilliporeSigma), pyridine (anhydrous, >99.8 wt%, MilliporeSigma) and 2-butanol (99.8 wt%, MilliporeSigma) were purified via successive freeze–pump-thaw cycles to remove dissolved gases. Prior to degassing 2-butanol, carbonyl impurities were removed by refluxing over sodium borohydride ($NaBH_4$, >95%, Macron Fine Chemicals) for 12 h and then distilling onto activated 3A molecular sieves to remove trace water [49]. Adsorbates were introduced to the transmission cell in serial doses (0.1–1.0 μmol per dose) using a Baratron capacitance manometer (0.01 Torr resolution; MKS Instruments) to monitor the pressure in the IR cell. A spectrum was measured after each dose once the pressure in the cell remained constant for > 30 s. All reported IR spectra were baseline-corrected and normalized by the total area of the T-O-T combination and overtone modes (2100–1750 cm^{-1}) of the parent spectrum. The number of Lewis acid sites counted by pyridine and CD_3CN was estimated from integrated IR peak areas and appropriate IMEC values (ε) using the following equation:

$$Lewis\ Acid\ Site\ Density = \left(\frac{Peak\ Area}{\varepsilon}\right) * \left(\frac{W_{CSA}}{g_{cat}}\right) \quad (1)$$

Where W_{CSA} and g_{cat} are the cross-sectional area and the mass of the zeolite pellet, respectively. Additional methods and details can be found in Sections S.3 (pyridine) and S.4 (CD_3CN) of the Supporting Information.

2.4. Measurement of MPVO kinetics

MPVO kinetic studies were performed following a previously described procedure [49]. Briefly, reactant solutions were prepared with varying concentrations of cyclohexanone (0.01–1 M; 99.5 wt %, MilliporeSigma) in a 2-butanol solvent (99.8 wt%, MilliporeSigma). Zeolite powder (~10 mg) and a PTFE-coated magnetic stir bar were loaded into glass batch reactors (10 cm^3, VWR Scientific), sealed with a PTFE-lined silicone septum in an aluminum crimp top (Supelco), and heated to 373 K in a magnetically stirred oil bath for > 15 min. ~ 2 cm^3 of the reactant solution was sealed in a separate glass batch reactor, preheated in an oil bath held at 373 K for > 15 min, and then transferred to the catalyst vial via gas-tight syringe where the reaction was allowed to proceed for 10 min. Reaction solutions were then quenched in an ice bath, filtered with a 0.2 μm PTFE syringe filter (VWR), and diluted with a

2-pentanone standard solution (5 wt% 2-pentanone in 2-butanol; 99.5 wt%, HPLC grade, MilliporeSigma). Filtered reaction solutions were then injected into a gas chromatograph (7890A, Agilent Technologies) equipped with a DB-1701 column (30 m × 250 μm × 0.25 μm, Agilent) and a flame ionization detector.

3. Results and discussion

3.1. Quantification of Lewis acidic Sn sites by pyridine adsorption

Lewis acid site counts determined by different basic titrants were first validated by measuring integrated molar extinction coefficients (IMECs) on Sn-Beta zeolites in order to benchmark site counts and MPVO turnover rates. Such quantitative kinetic benchmarking serves to validate the direct comparison of MPVO rate data reported here on both Sn- and Hf-Beta zeolites using established literature precedent to quantify Lewis acid sites in Beta zeolites. IMECs for pyridine and CD_3CN adsorbed at Lewis acid sites were determined using a similar method to that described by Emeis [52] and Harris et al. [32] Infrared spectra were collected with increasing coverages of pyridine on three hydrophobic Sn-Beta samples with Si/Sn molar ratios ranging from 151 to 298 and are shown in Fig. 1.

At low pyridine coverages (pyridine/Sn < 0.30), the IR spectra showed two peaks centered near 1451 cm^{-1} and 1611 cm^{-1} that are characteristic of the perturbed deformation modes of pyridine bound to Lewis acid sites. The intensities of both these signals increased linearly up to saturation with increasing pyridine coverage (Figure S7, SI). Additional peaks centered near 1491 cm^{-1} and 1578 cm^{-1}, which reflect ring stretching modes of pyridine coordinated to either Lewis or Brønsted acid sites, were also observed at low pyridine coverages [53,54]. At elevated pyridine coverages, peaks characteristic of gaseous or physisorbed pyridine were observed near 1440 cm^{-1} and 1594 cm^{-1} and increased in intensity after saturation of accessible Lewis acid sites. IR peaks arising solely due to protonated pyridine (1550 cm^{-1} and 1637 cm^{-1}) [53,54] were absent in all spectra (Fig. 1), indicating the absence of Brønsted acid sites in these Sn-Beta samples. Integrated peak areas of pyridine bound at Lewis acid sites (1451 cm^{-1} and 1611 cm^{-1}) with substoichiometric coverages (pyridine/Sn < 0.90) increased linearly with pyridine coverage on the three Sn-Beta samples (Fig. 2). Note that while the integrated peak areas increase linearly, there is a noticeable intercept due to a small fraction (0.11 μmol) of pyridine sticking to the inside of the IR cell. This residual amount of adsorbed pyridine represented <10% of the total pyridine adsorbed on Lewis acid sites at saturation during a typical experiment. Further, this amount was the same across all samples investigated here, independent of framework metal identity (*vide infra*), and appeared to only affect the amount of pyridine adsorbed in the very first dose. As a result, the residual amount of pyridine adsorbed in the cell did not affect the determination of pyridine Lewis acid site counts as the measured slope (i.e., IMEC) is independent of the initial dose.

The integrated IR band area increased with the same slope of 1.58 ± 0.16 cm μmol^{-1} on all three Sn-Beta samples (Fig. 2), thus representing the IMEC (ε(Sn; 1451 cm^{-1})) for this vibrational mode. This value is similar to those previously reported for pyridine bound to Lewis acidic Sn sites in Beta zeolites (ε(Sn; 1451 cm^{-1}): 1.42 ± 0.30 cm μmol^{-1}) [32] and within the range reported for pyridine adsorbed at other Lewis acid sites in crystalline and amorphous oxides (ε(1451 cm^{-1}): 0.89–3.9 cm μmol^{-1}) [32,36,52,55,56]. Infrared spectra were collected on three additional Sn-Beta samples after saturation with pyridine at 423 K (Figures S8-S10, SI) and integrated IR peak areas, together with the ε (Sn; 1451 cm^{-1}) value determined from spectra collected at substoichiometric coverages (pyridine/Sn < 0.9; Fig. 2), were used to determine the number of Lewis acidic Sn sites. The total number of Lewis acid sites normalized per total Sn measured by ICP-MS (LAS/Sn) on all Sn-Beta samples, regardless of Sn content or synthesis method (i.e., direct crystallization with F^- or solvent-assisted grafting), varied between 0.63 and 1.00 (see Table 1). Sn-Beta samples with LAS/Sn < 0.80 also showed detectable amounts of SnO_x domains in UV–Vis spectra after dehydration at 523 K (Figure S3, SI), consistent with the preferential titration of tetrahedral Lewis acid sites by pyridine under the conditions used here.

3.2. Quantification of Lewis acidic Sn sites by CD_3CN

Infrared spectra were also measured on Sn-Beta zeolites with increasing coverages of CD_3CN at 303 K and deconvoluted into principle component peaks using deconvolution methods described previously [32,49]. Consistent with prior observations, a peak centered near 2316 cm^{-1} was observed at low CD_3CN coverages (CD_3CN/Sn < 0.3; Fig. 1), corresponding to the preferential adsorption of CD_3CN at open Sn sites. With increasing coverage this peak center red-shifted towards 2308 cm^{-1} due to subsequent adsorption of CD_3CN at closed Sn sites [27–29,32]. At elevated coverages of CD_3CN, additional peaks were observed that can be ascribed to adsorption at silanol groups (SiOH, 2275 cm^{-1}) [57] and gaseous or physisorbed CD_3CN (2265 cm^{-1}). In some Sn-Beta samples (e.g., Sn-Beta-F(298)), an additional peak centered near 2288 cm^{-1} was observed at low CD_3CN coverages (CD_3CN/Sn < 0.4), which has been previously attributed to CD_3CN coordination at highly defective Sn sites (e.g., $Sn(OH)_2(OSi)_2$; Fig. 1c) [32,37,58,59]. As a result, this additional component peak was included in the deconvolution of all IR spectra of CD_3CN adsorbed on Sn-Beta (additional details can be found in Section S.4 of the SI). Peak areas associated with open Sn sites (2316 cm^{-1}) saturated at substoichiometric coverages of CD_3CN (CD_3CN/Sn < 0.5, Figure S26, SI), while saturation of closed Sn sites occurred around coverages of CD_3CN/Sn ∼ 1.5 due to concurrent adsorption of CD_3CN at silanol groups after saturation of open Sn sites.

Non-linear regression was used to determine the IMEC values for open (ε(Sn; 2316 cm^{-1})) and closed (ε(Sn; 2308 cm^{-1})) Sn sites that would result in the same total number of Lewis acid sites counted by either pyridine or CD_3CN. This procedure resulted in values of ε(Sn; 2316 cm^{-1}) and ε(Sn; 2308 cm^{-1}) of 1.80 ± 0.25 cm μmol^{-1} and 3.76 ± 0.33 cm μmol^{-1}, respectively, which are both ∼ 1.8x larger than those reported previously for CD_3CN adsorbed on Sn-Beta [32]. A contour plot of the least-squares regression error calculated as a function of the values of ε(Sn; 2316 cm^{-1}) and ε(Sn; 2308 cm^{-1}) showed that there was a singularly unique solution that minimized the global fitting error during the CD_3CN IMEC regression procedure (Figure S24, SI). We validated these CD_3CN IMECs by comparing the total number of Lewis acid sites counted by CD_3CN and pyridine on three additional Sn-Beta zeolites not used in the initial determination of CD_3CN IMEC values. The number of Lewis acid sites were within 1.2x (Fig. 3, Table 1) on all Sn-Beta samples investigated. These results provide additional evidence that the values of ε(Sn; 2316 cm^{-1}) and ε(Sn; 2308 cm^{-1}) reported here reasonably estimate the total number of Lewis acidic Sn sites in Beta zeolites under the specific conditions and experimental setup reported here.

While the values reported here for CD_3CN IMECs on Sn sites in Beta zeolites differ from those previously reported by Harris et al. [32], they are similar to those reported for Ti Lewis acid sites in Beta zeolites (ε(Ti; 2308 cm^{-1}): 3.01 ± 0.60 cm μmol^{-1}) [36] and Lewis acidic Al species in FER-type zeolites (ε(Al; 2325 cm^{-1} or 2310 cm^{-1}): 3.6 ± 0.2 cm μmol^{-1}) [57]. To further assess these differences, the IMEC for CD_3CN adsorbed on silanol groups (ε (2275 cm^{-1})) was determined via quantitative dosing of CD_3CN

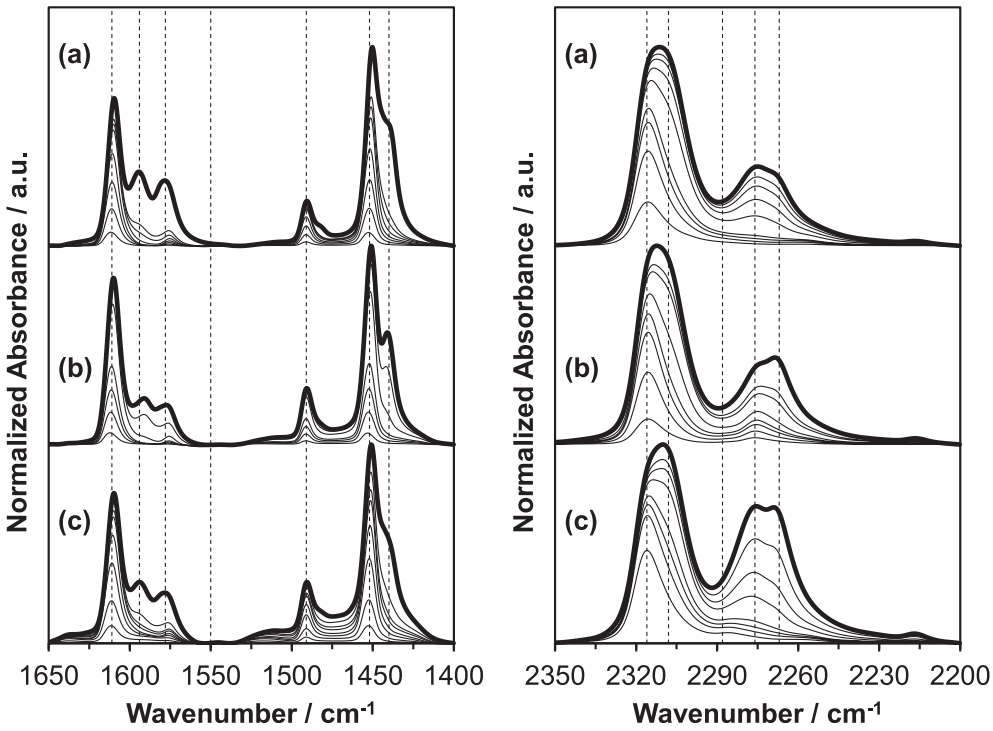

Fig. 1. IR spectra, normalized by their maximum intensity, measured as a function of pyridine (left) and CD_3CN (right) coverage (saturated spectra are bolded lines) for (a) Sn-Beta-F(188), (b) Sn-Beta-F(151), and (c) Sn-Beta-F(298). Dashed lines show the positions of vibrational modes for pyridine coordinated to Lewis acid sites (1611 cm^{-1}, 1451 cm^{-1}), Lewis or Brønsted acid sites (1578 cm^{-1}, 1491 cm^{-1}), Brønsted acid sites (1550 cm^{-1}), and gas-phase pyridine (1440 cm^{-1}, 1594 cm^{-1}), and CD_3CN bound to open Sn sites (2316 cm^{-1}), closed Sn sites (2308 cm^{-1}), defective Sn sites (e.g., $Sn(OSi)_2(OH)_2$; 2288 cm^{-1}), silanol groups (2276 cm^{-1}), and gaseous CD_3CN (2267 cm^{-1}).

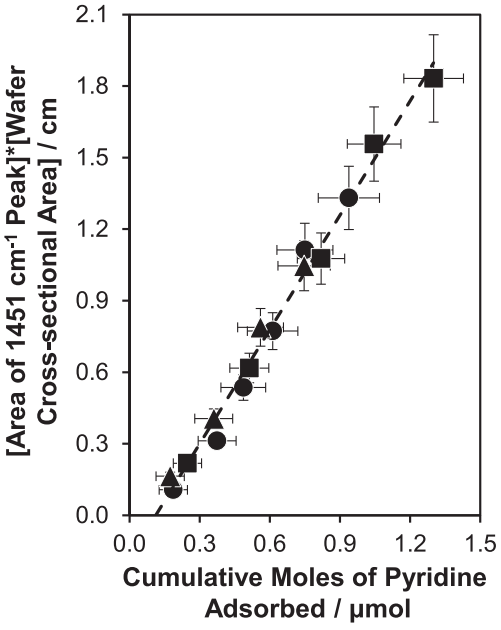

Fig. 2. Integrated IR peak area (1451 cm^{-1}) corresponding to pyridine/Sn coverages between 0.1 and 0.8 on Sn-Beta-F(298) (triangles), Sn-Beta-F(151) (circles), Sn-Beta-F(188) (squares) used to determine the IMEC of pyridine adsorbed on Lewis acid sites (1451 cm^{-1}) from Eq. (1) upon multiplication of pellet mass to both sides of the equation. Error bars reflect propagated experimental uncertainties.

onto dealuminated Beta (Si-Beta-OH, Si/Al > 5000). A value of 1.3 5 ± 0.12 cm μmol^{-1} was determined for ε(2275 cm^{-1}) (Figure S27, SI), which is ca. 1.8x larger than that reported previously for CD_3CN adsorbed on silanol groups in dealuminated-Beta zeolites (ε (2275 cm^{-1}): 0.74 ± 0.16 cm μmol^{-1}) [32]. Unlike the values for ε(Sn; 2316 cm^{-1}) and ε(Sn; 2308 cm^{-1}), which were fit such that the total Lewis acid sites counted by CD_3CN matched that determined from pyridine adsorption, the value of ε(2275 cm^{-1}) was determined directly from calibrated doses of CD_3CN that selectively adsorb on silanol groups in Si-Beta-OH (Figure S27, SI) [60]. Moreover, differences between the pyridine IMEC for Lewis acid bound pyridine reported here (1.58 cm μmol^{-1}) and that reported by Harris et al. (1.42 cm μmol^{-1}) are < 1.15x different, suggesting that differences in measured CD_3CN IMECs are likely not due to systematic experimental errors, but rather due to variability in acquisition parameters or spectrometer optics that give rise to differences in peak areas (or lineshapes) for a similar analyte composition. Such differences in spectral lineshapes, which may lead to changes in peak areas or signal response, can arise for several reasons including (but not limited to) nonlinear detector response as a function of photon energy, differences in how the raw interferogram is processed into an absorbance spectrum, and optical distortions due to reflectance, fluorescence, or imperfections at optical interfaces [61–65]. This, to some extent, may explain the wide range in IMECs reported in the open literature for Lewis acid bound pyridine (ε(1450 cm^{-1}): 0.89–3.9 cm μmol^{-1}) [32,52,56] and further emphasizes the critical importance of benchmarking active site counts against robust, well-established experimental protocols and, where possible, using multiple titrants for independent validation [66].

Further validation of the number of open and closed Lewis acidic Sn sites was performed by measuring the rate of the MPVO reaction between cyclohexanone and 2-butanol on a series of Sn-Beta zeolites (see Section S.5 of the SI). This reaction was chosen because intermolecular MPVO reactions are putatively catalyzed only by the open metal sites in Lewis acid zeolites [27,37,41,67,68]. Apparent zero-order MPVO rate constants (per gram catalyst, 373 K) were measured on three hydrophobic (Sn-Beta-F) and three hydrophilic (Sn-Beta-OH) zeolites and were ~ 5x larger on hydrophobic than hydrophilic Sn-Beta zeolites, consistent with previous observations for liquid-phase MPVO

Table 1
Sn content, total number of Lewis acid sites normalized per total Sn measured by ICP-MS (LAS/Sn), open/closed Sn site ratios, and total number of SiOH groups determined from IR spectra of adsorbed pyridine and CD_3CN on different Sn-Beta zeolites.

Sample	Si/Sn	LAS/Sn (Pyridine)	LAS/Sn (CD_3CN)	Open/Closed	SiOH Content/μmol g^{-1}
Sn-Beta-F(298)	298	1.00 ± 0.10	1.01 ± 0.14	0.60	39.9
Sn-Beta-F(151)	151	0.63 ± 0.07	0.62 ± 0.09	0.93	97.1
Sn-Beta-F(188)	188	0.88 ± 0.09	0.88 ± 0.12	1.01	44.1
Sn-Beta-F(81)	81	0.74 ± 0.13	0.75 ± 0.15	0.71	65.7
Sn-Beta-F(219)	219	0.99 ± 0.12	0.84 ± 0.13	0.48	85.6
Sn-Beta-OH(337)	337	0.73 ± 0.13	0.70 ± 0.14	0.52	671

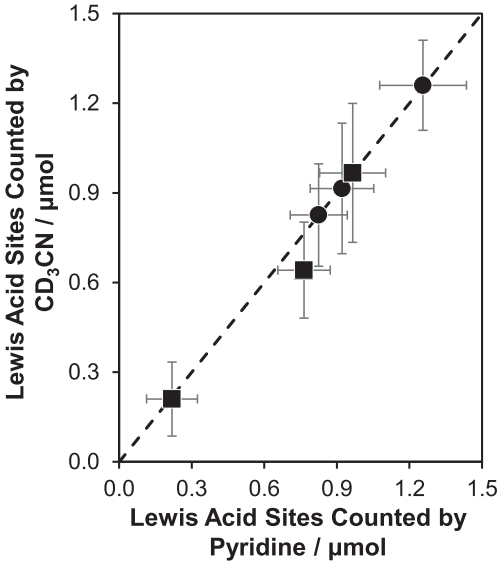

Fig. 3. Number of Lewis acidic Sn sites counted by pyridine and CD_3CN on six different Sn-Beta zeolites with Si/Sn = 81–337. Circles represent samples used for the fitting of CD_3CN IMECs and squares are three additional Sn-Beta samples not used in IMEC fitting. The dashed line is a parity line. Error bars reflect propagated experimental uncertainties.

catalysis [32,36,49,69]. Regardless of differences in free energy barriers associated with the intraporous solvent structure [36,49,70], rate constants on both series of Sn-Beta zeolites correlated with the total number of open Sn sites (2316 cm^{-1}, per gram), but not with the number of closed Sn sites (2308 cm^{-1}; Figure S37, SI). This result is consistent with a wide body of literature reporting that open Lewis acid sites are the active site for MPVO transfer hydrogenation reactions [27,28,32,41,71] and further supports the CD_3CN IMECs reported here. These results underscore the importance of benchmarking site counts and kinetic measurements through independent verification prior to reporting turnover rate measurements on new site ensembles.

3.3. Quantification of Lewis acidic Hf sites by pyridine titration

Most comparative studies on Hf-containing zeolites rely on rate normalizations on a per total metal basis, thereby masking any quantitative relationship between catalytic performance and active site identity [37,38,41–44,72–76]. A faithful comparison of catalytic turnover rates between different Hf-containing zeolite catalysts, or with zeolites containing other heteroatoms, requires that reaction rates be normalized by the number of sites that catalyze such reactions. Having established rigorous protocols for counting distinct sites in Sn-Beta, we determined the IMEC of pyridine bound to Lewis acidic Hf sites (ε(Hf; 1450 cm^{-1}) by collecting IR spectra with increasing coverages of pyridine on three separate Hf-Beta zeolites with different Hf content (Si/Hf = 100–413; Fig. 4). IR spectra measured at low pyridine coverages (pyridine/Hf < 0.40) showed two peaks centered near 1448 cm^{-1} and 1608 cm^{-1}, characteristic of the perturbed deformation modes of pyridine bound to Lewis acid sites, that increased in area linearly prior to saturation (Figure S11, SI). Peak centers for pyridine bound to Lewis acidic Hf sites were red-shifted by ~ 3 cm^{-1} compared to similar vibrational peaks observed for pyridine adsorbed on Sn-Beta zeolites (Fig. 1), likely due to differences in the strength of acid-base interactions that perturb pyridine ring vibrations from those observed in the gas-phase. Additional peaks centered near 1491 cm^{-1} and 1576 cm^{-1}, which reflect pyridine coordinated to either Lewis or Brønsted acid sites, were also observed. With increasing pyridine coverage, peaks characteristic of gaseous or physisorbed pyridine were observed near 1440 cm^{-1} and 1593 cm^{-1} and increased in intensity after saturation of accessible Lewis acid sites (Figure S11, SI). Similar to our observations on Sn-Beta (Fig. 1), IR peaks arising solely due to protonated pyridine (1550 cm^{-1} and 1637 cm^{-1}) were absent in all spectra (Fig. 4), indicating the absence of Brønsted acid sites on Hf-Beta zeolites investigated here.

Integrated peak areas of pyridine bound to Lewis acid sites (1448 cm^{-1} and 1608 cm^{-1}) with substoichiometric coverages (pyridine/Hf < 0.80) increased linearly with pyridine coverage on these three Hf-Beta samples (Fig. 5). As seen previously with pyridine adsorption on Sn-Beta (Fig. 2), there is a small amount of excess pyridine adsorbed on the cell (0.08 μmol) during the initial pyridine dose on Hf-Beta, but this value is the same across all Hf-Beta samples investigated here and is similar in total amount to that observed during pyridine dosing on Sn-Beta (0.11 μmol). This residual adsorption on the IR cell does not affect the determination of the IMEC or the quantification of the number of Lewis acidic Hf sites in Hf-Beta zeolites at saturation. The integrated IR band area of pyridine adsorbed on Hf Lewis acid sites increased with the same slope of 1.54 ± 0.21 cm $μmol^{-1}$ on all three Hf-Beta samples (Fig. 5), and represents the IMEC for pyridine adsorbed on Hf Lewis acid sites (ε(Hf; 1448 cm^{-1})). The value of ε(Hf; 1448 cm^{-1}) is consistent with our measurement of ε(Sn; 1451 cm^{-1}) = 1.58 ± 0.16 c m $μmol^{-1}$ and IMECs reported for pyridine bound to Lewis acid sites in solid oxides (ε(1450 cm^{-1}): 0.89–3.9 cm $μmol^{-1}$) [32,36,52,55,56]. Infrared spectra of adsorbed pyridine were also collected on five additional Hf-Beta samples after saturation at 423 K (Figures S12-S16 in the SI). The total number of Lewis acid sites (per total Hf) on all Hf-Beta samples, regardless of Hf content or synthesis method, varied between 0.60 and 1.38 (Table 2). Pyridine appears to selectively bind to tetrahedral Lewis acid sites in the presence of extraframework HfO_x domains, as Hf-Beta samples containing oligomeric Hf species, observable from UV–Vis spectra (Figure S4, SI), had total Lewis acid site counts (per total Hf) less than unity. Moreover, IR spectra of pyridine adsorbed on a Si-Beta-F sample impregnated with HfO_x (HfO_x/Si-Beta-F, Si/Hf = 100; Figure S17, SI) showed that only a small fraction of all Hf atoms exist as Lewis acid sites (LAS/Hf = 0.14), suggesting that the majority of Hf sites in HfO_x clusters do not appreciably bind with or are inaccessible to pyridine. Based on these observations, we concluded that pyridine is an adequate probe to quantify the total number of Lewis acidic sites in Hf-Beta zeolites even in the presence of oligomeric HfO_x moieties.

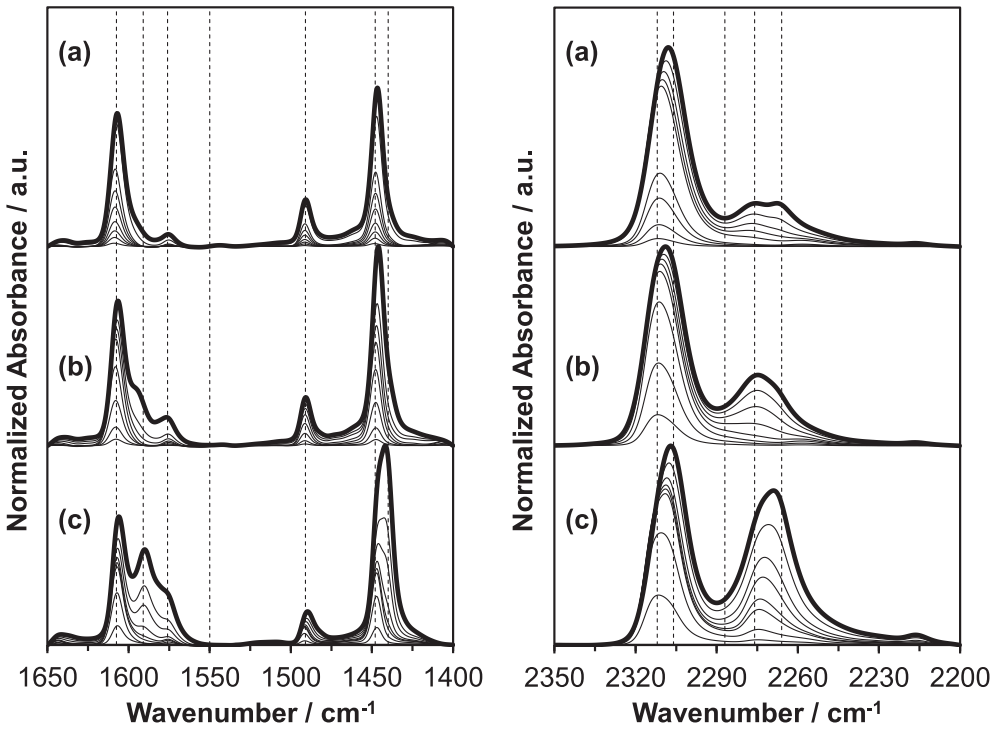

Fig. 4. IR spectra, normalized by their maximum intensity, measured as a function of pyridine (left) and CD_3CN (right) coverage (saturated spectra are bolded lines) for (a) Hf-Beta-F(100), (b) Hf-Beta-F(199), and (c) Hf-Beta-F(413). Dashed lines show the positions of vibrational modes for pyridine coordinated to Lewis acid sites (1608 cm^{-1}, 1448 cm^{-1}), Lewis or Brønsted acid sites (1577 cm^{-1}, 1491 cm^{-1}), Brønsted acid sites (1550 cm^{-1}), and gas-phase pyridine (1440 cm^{-1}, 1593 cm^{-1}), and CD_3CN bound to open Hf sites (2313 cm^{-1}), closed Hf sites (2307 cm^{-1}), defective Hf sites (e.g., $Hf(OSi)_2(OH)_2$; 2287 cm^{-1}), silanol groups (2276 cm^{-1}), and gaseous CD_3CN (2266 cm^{-1}).

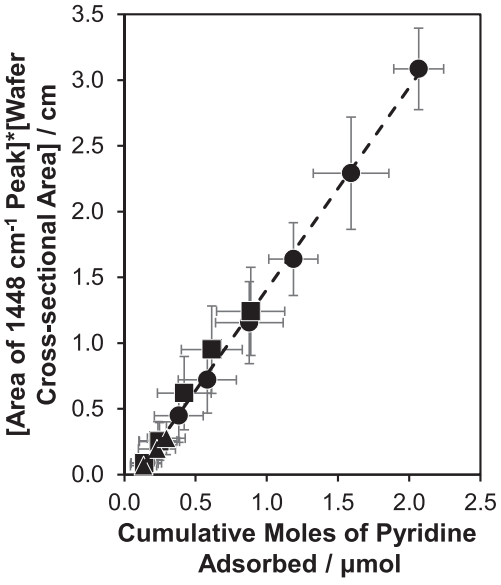

Fig. 5. Determination of the IMEC for pyridine adsorbed on Lewis acid sites (1448 cm^{-1}) on Hf-Beta-F(413) (triangles), Hf-Beta-F(100) (circles), Hf-Beta-F(199) (squares) from integrated IR peak areas corresponding to pyridine/Sn coverages between 0.1 and 0.8. Error bars reflect propagated experimental uncertainties.

3.4. Quantification of open and closed Lewis acidic Hf sites by CD_3CN titration

IMECs based on CD_3CN adsorption were calculated for open (2312 cm^{-1}) and closed (2306 cm^{-1}) Hf sites (based on previous assignments using a combination of DFT methods and adsorption spectra measured after saturation with CD_3CN (static 2 mbar at 298 K)) [38]. Specifically, three separate Hf-Beta zeolites (Si/Hf = 100–413) were exposed to calibrated amounts of CD_3CN and IR spectra were measured at various coverages of CD_3CN (0.1–5.9 CD_3CN/Hf; Fig. 4). IR spectra of CD_3CN adsorbed on Hf-Beta at low coverages (CD_3CN/Hf < 0.3) showed an asymmetric peak centered near 2312 cm^{-1} that grew in intensity with increasing CD_3CN coverage and red-shifted towards 2308 cm^{-1} near saturation (Fig. 4). With increasing amounts of CD_3CN adsorbed, peaks characteristic of CD_3CN bound to SiOH groups (2276 cm^{-1}) and gaseous CD_3CN (2266 cm^{-1}) were observed that grew in intensity as the equilibrium pressure of CD_3CN increased. These observations suggest that two different Lewis acidic Hf sites likely exist on Hf-Beta zeolites and the apparent peak positions are consistent with ν(C≡N) vibrational modes calculated from DFT for CD_3CN adsorbed on closed (2306 cm^{-1}) and open (2312 cm^{-1}) Hf sites [38]. This shift in vibrational frequency at elevated CD_3CN coverages on Hf-Beta is not as pronounced as that seen for CD_3CN adsorption on Sn-Beta (Fig. 1; Sn: 8 cm^{-1}, and Fig. 4; Hf: 4 cm^{-1}). The spectra near saturation resemble those of CD_3CN adsorbed on Ti- and Zr-Beta zeolites, where only a single Lewis acid site has been identified by IR spectra of adsorbed CD_3CN [36,46].

Analysis of the second derivative IR absorbance spectrum further confirmed the presence of two component peaks for CD_3CN bound to Lewis acidic Hf sites. Indeed, the second derivative analysis of the absorbance spectrum on three different Hf-Beta samples revealed the presence of two overlapping component peaks in the region between 2300 and 2320 cm^{-1}. These features were identified by distinct local minima in the second derivative and are centered near 2313 cm^{-1} and 2307 cm^{-1} with two additional peaks found near 2276 cm^{-1} and 2266 cm^{-1} (Fig. 6). The peak centers are consistent with previous conclusions that Hf-Beta contains two distinct Lewis acid sites distinguishable in IR spectra after titration with CD_3CN [38]. This analysis was further validated by calculating the second derivative of the absorbance spectrum for

Table 2
Hf content, total number of Lewis acid sites per total Hf (LAS/Hf), open/closed Hf site ratios, and total number of SiOH groups determined from IR spectra of adsorbed pyridine and CD_3CN on different Hf-Beta zeolites.

Sample	Si/Hf	LAS/Hf (Pyridine)	LAS/Hf (CD_3CN)	Open/Closed	SiOH Content/μmol g^{-1}
Hf-Beta-F(413)	413	0.95 ± 0.13	0.99 ± 0.23	0.41	23.1
Hf-Beta-F(100)	100	0.71 ± 0.12	0.71 ± 0.09	0.32	28.5
Hf-Beta-F(199)	199	0.96 ± 0.11	0.95 ± 0.18	0.47	50.0
Hf-Beta-OH(109)	109	0.73 ± 0.09	0.69 ± 0.14	0.38	517
Hf-Beta-F(154)	154	1.17 ± 0.16	1.35 ± 0.18	0.76	87.2
Hf-Beta-F(285)	285	1.07 ± 0.18	0.90 ± 0.17	0.44	51.5
Hf-Beta-F(308)	308	1.38 ± 0.28	1.00 ± 0.20	0.60	59.5
Hf-Beta-F(102)	102	0.60 ± 0.13	0.54 ± 0.15	0.44	189

CD_3CN adsorbed on Sn, Zr, and Ti-Beta-F zeolites (Figure S18, SI). Consistent with previous observations, Ti- and Zr-Beta zeolites appear to only contain a single Lewis acid site distinguishable by CD_3CN (centered near 2307 cm^{-1} and 2305 cm^{-1}, respectively) [36,46], while two peaks are clearly resolved for CD_3CN adsorbed on open and closed sites in Sn-Beta zeolites (2316 cm^{-1} and 2308 cm^{-1}, respectively) [27,32]. Recent work from Bates and co-workers further assigned the peak at 2316 cm^{-1} to Sn sites located in the grain boundaries of Beta zeolites through a combination of ethanol dehydration kinetics, in-situ titrations, and computational modelling [23]. While our analysis provides evidence for the presence of two distinct Lewis acidic Hf sites in Hf-Beta zeolites that are tentatively assigned to open (e.g., $HfOH(OSi)_3$; 2313 cm^{-1}) and closed (e.g., $Hf(OSi)_4$; 2307 cm^{-1}) Hf sites, sites arising from the 2313 cm^{-1} feature may similarly locate at stacking faults within the Beta zeolite.

A fifth feature was also observed at low coverages of CD_3CN adsorbed on some Hf-Beta zeolites (CD_3CN/Hf < 0.6, Fig. 4) and on HfO_x/Si-Beta-F(100) (Figure S20, SI) as a small shoulder with a peak center near 2288 cm^{-1}. This is reminiscent of features characteristic of CD_3CN adsorbed on highly defective Sn species observed on Sn-Beta zeolites, and has previously been observed in IR spectra of CD_3CN adsorbed on Hf-Beta zeolites [38]. Therefore, this component was included during the deconvolution of all IR spectra of CD_3CN adsorbed on Hf-Beta zeolites. Peak areas associated with "open" Hf sites (2313 cm^{-1}) reach saturation at substoichiometric coverages of CD_3CN on Hf-Beta-F(100) (CD_3CN/Hf < 0.25, Fig. 7), while saturation of "closed" Hf sites occurs near coverages of CD_3CN/Hf ~ 1, suggesting that CD_3CN binds with a 1:1 stoichiometry to Lewis acidic Hf sites in Beta zeolites before adsorption at other binding sites (e.g., SiOH groups).

At CD_3CN/Hf coverages exceeding 0.5, appreciable adsorption of CD_3CN at silanol groups was observed, as well as an increase in the amount of gaseous CD_3CN. IMECs for open (ε(Hf; 2313 cm^{-1})) and closed (ε(Hf; 2307 cm^{-1})) Hf sites were determined by nonlinear regression such that both CD_3CN and pyridine counted the same number of Lewis acid sites on three separate Hf-Beta zeolites. This procedure resulted in values of ε(Hf; 2313 cm^{-1}) and ε(Hf; 2307 cm^{-1}) of 2.40 ± 0.22 cm μmol^{-1} and 3.55 ± 0.41 cm μmol^{-1}, respectively, which are similar to the values we obtained for open and closed Sn sites in Beta zeolites (ε(Sn; 2316 cm^{-1}): 1.80 ± 0.2 5 cm μmol^{-1} and ε(Sn; 2308 cm^{-1}): 3.76 ± 0.33 cm μmol^{-1}). The uniqueness of these values was assessed using a contour plot of the least-squares regression error calculated as a function of the values of ε(Hf; 2313 cm^{-1}) and ε(Hf; 2307 cm^{-1}) showing a single solution that minimizes the global fitting error during the CD_3CN IMEC regression (Figure S25, SI). Further validation of the CD_3CN IMECs for Lewis acidic Hf sites was performed by comparing the total number of Lewis acid sites counted by CD_3CN and pyridine on five additional Hf-Beta zeolites not used in the initial determination of CD_3CN IMEC values. The number of sites counted by both titrants was within 1.4x (Fig. 8, Table 2) on all Hf-Beta samples investigated providing additional evidence that CD_3CN also binds with equimolar stoichiometry at Lewis acidic Hf sites. Moreover, these data indicate that both pyridine and CD_3CN can be used to quantify the total number of Lewis acidic Hf sites in Hf-Beta zeolites from IR spectra after saturation with either titrant.

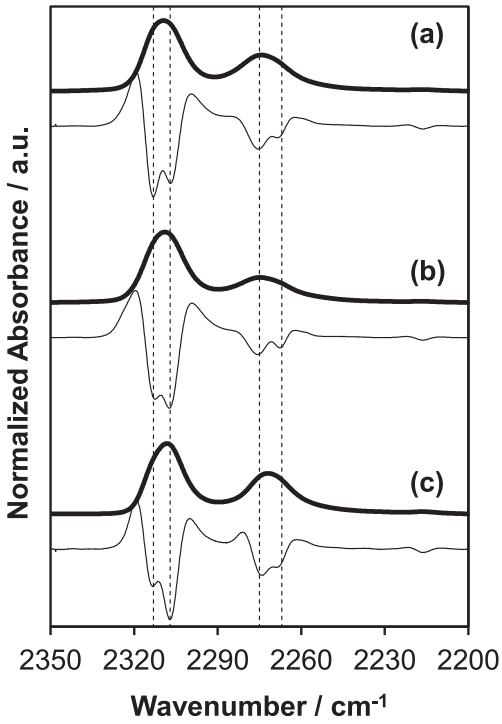

Fig. 6. IR absorbance (bold) and second derivative spectra (thin) of CD_3CN adsorbed on (a) Hf-Beta-F(100), (b) Hf-Beta-F(199), and (c) Hf-Beta-F(413) at 303 K after saturation. Dashed lines show identified peak centers at 2313 cm^{-1}, 2307 cm^{-1}, 2276 cm^{-1}, and 2266 cm^{-1}.

As seen for CD_3CN adsorption on Sn-Beta samples [32], the open/closed ratio decreased systematically with increasing coverage of CD_3CN, consistent with the preferential adsorption of CD_3CN at open Hf sites prior to adsorption at closed Hf sites (Figure S28, SI). The ratio of open to closed Hf Lewis acid sites (Table 2) was, on average, lower than that observed for Sn-Beta samples (Table 1), suggesting that Hf is more readily incorporated at locations within the Beta framework that favor the formation of four bonds with lattice O atoms [23]. Precise conclusions regarding the preferential occupancy of different positions within the zeolite lattice, however, require synthesis methods that can selectively bias the placement of heteroatoms throughout the zeolite framework [24]. Instead, we investigated the catalytic function of these different Lewis acidic Hf sites for the hydrogenation of cyclohexanone using 2-butanol as a hydrogen donor.

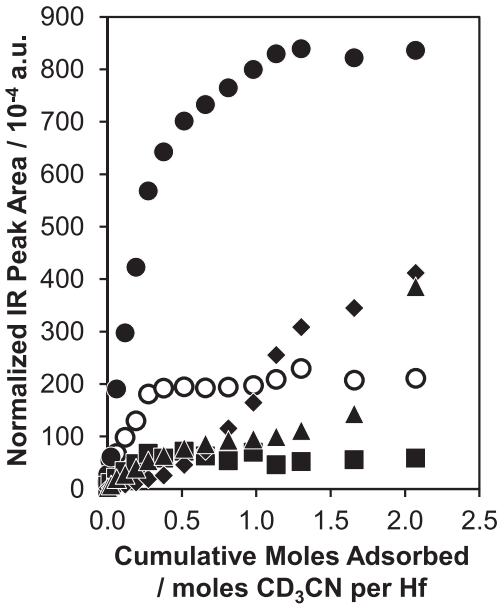

Fig. 7. Integrated IR peak areas determined as a function of CD_3CN coverage on Hf-Beta-F(100) for CD_3CN bound to open Hf sites (2313 cm^{-1}, open circles), closed Hf sites (2307 cm^{-1}, solid circles), defective Hf sites (2288 cm^{-1}, squares), silanol groups (2276 cm^{-1}, diamonds), and gaseous CD_3CN (2267 cm^{-1}, triangles).

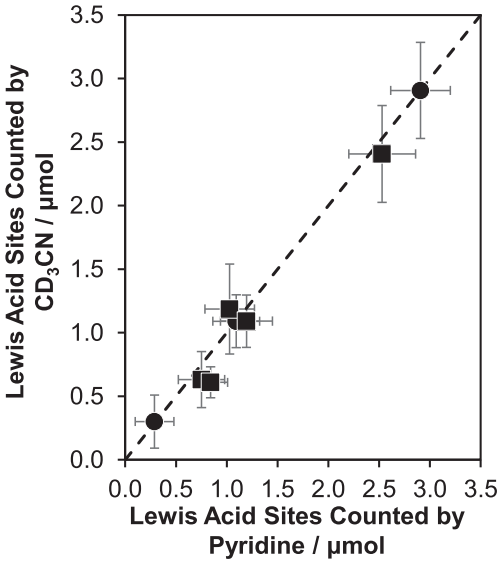

Fig. 8. Number of Lewis acidic Hf sites counted by pyridine and CD_3CN on 8 different Hf-Beta zeolites with Si/Hf = 100–413. Circles represent samples used for the fitting of CD_3CN IMECs and squares are five additional Hf-Beta samples not used in IMEC fitting. Dashed line is a parity line. Error bars reflect propagated experimental uncertainties.

3.5. Identification of the MPVO active site on Hf-Beta zeolites

Initial cyclohexanol formation rates (normalized per total Hf, 373 K) were measured as a function of cyclohexanone activity (a_c; 0.01–1 M cyclohexanone) in a 2-butanol solvent on six Hf-Beta-F samples spanning Si/Hf ratios between 100 and 413. Cyclohexanol formation rates increased with a first-order dependence on cyclohexanone activity at low values of a_c (Fig. 9; full data set in Figure S38 of the SI) consistent with previous kinetic studies performed at low ketone concentrations in an alcohol solvent on Lewis acidic Beta zeolites [41,49].

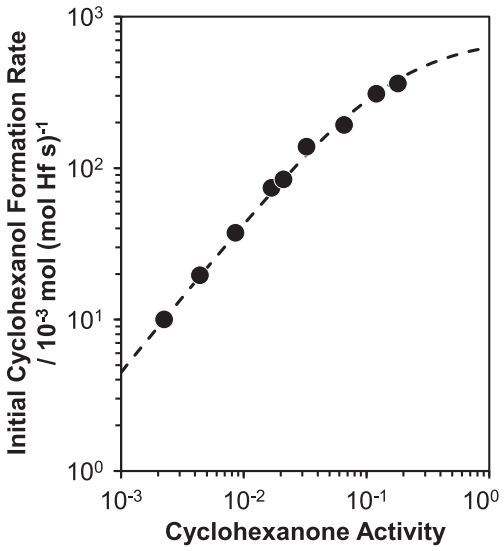

Fig. 9. Initial cyclohexanol formation rate (per total Hf) measured as a function of cyclohexanone activity on Hf-Beta-F(100) at 373 K in a 2-butanol solvent.

At higher values of a_c, cyclohexanol formation rates transitioned towards a zero-order kinetic regime (Fig. 9) consistent with the rate expression that describes MPVO catalysis in Sn-Beta zeolites (Eq. (2); details in Section S.5 of the SI), where the most abundant reactive intermediate (MARI) shifts from a 2-butanol covered site to a coadsorbed 2-butanol-cyclohexanone adduct [49].

$$\frac{r}{[L]} = \frac{K_{ads}k_{app}a_c}{a_B + K_{ads}a_C} \quad (2)$$

Here, K_{ads} represents the equilibrium constant for the adsorption of cyclohexanone, k_{app} is the apparent rate constant, a_i are the activities of 2-butanol (a_B) and cyclohexanone (a_C) in solution, and [L] is the concentration of open sites (i.e., active sites). Apparent first ($K_{ads}k_{app}$) and zero-order (k_{app}) MPVO rate constants, normalized by the total number of Hf sites, were extracted from initial rate data using Eq. (2) and varied up to ~ 5x between different Hf-Beta-F samples with no systematic correlation with Si/Hf ratio (Figure S39, SI). These results suggest that not all Hf sites catalyze MPVO reactions with the same turnover rate (or at all) and that a subset of sites is likely responsible for the observed catalytic behavior of these zeolites.

To better understand the site requirements for MPVO catalysis on Hf-Beta, apparent first- and zero-order rate constants (per total Hf, 373 K) were plotted against the number of open (ν(C≡N): 2313 cm^{-1}, Fig. 10), closed (ν(C≡N): 2307 cm^{-1}, Figure S40, SI), and total Lewis acidic Hf sites (Figure S41, SI) per total Hf content on each zeolite. Both first and zero-order rate constants (per Hf, 373 K) increased linearly with the total number of open Hf sites (i.e., ν(C≡N): 2313 cm^{-1}) with intercepts that passed near the origin (Fig. 10). This trend was not observed when rate constants were plotted against the number of closed Hf sites (i.e., ν(C≡N): 2307 cm^{-1}; Figure S40, SI) or total number of Lewis acid sites (Figure S41, SI), which showed significant x-intercepts suggesting these site counts do not represent the active Hf site for this reaction. Notably, since cyclohexanone concentrations were kept < 1 M across all experiments to avoid modifying the solvent properties of 2-butanol, the full zero-order regime was difficult to sample, resulting in a weaker correlation in the apparent zero-order rate constant (Fig. 10b). This correlation of rates with the number of open Hf sites ν(C≡N): 2313 cm^{-1}) was observed across a broad range of open/closed site ratios (open/closed = 0.32–0.76) and without any systematic correlation between the amount of Hf

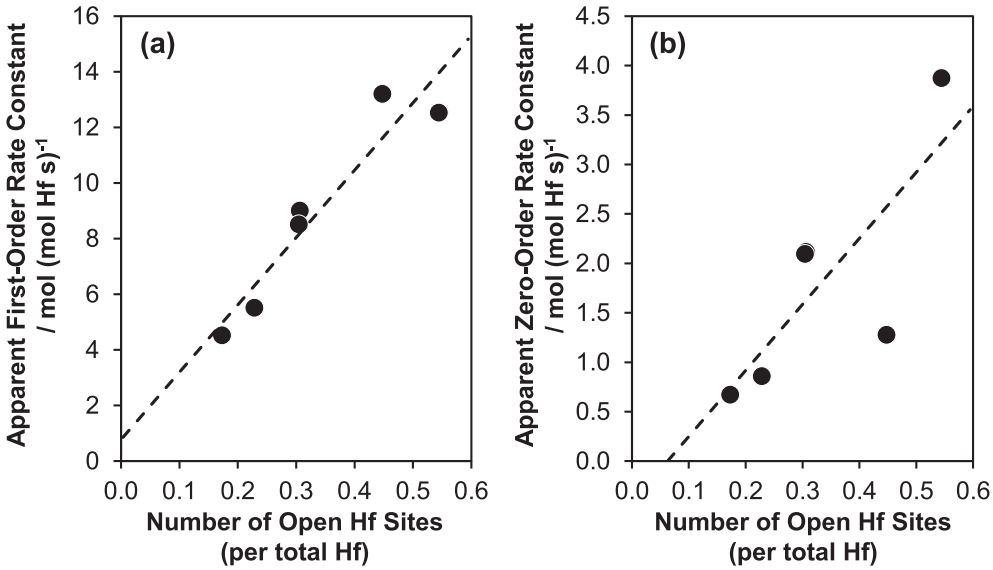

Fig. 10. Apparent first-order (a) and zero-order (b) MPVO rate constants (per total Hf, 373 K) as a function of the total number of open Hf sites (2313 cm^{-1}, per total Hf). Dashed lines represent linear regressions to the data sets.

on each sample or the number of open Hf sites (Table 2). Moreover, the presence of extraframework Hf species, observed predominately in Hf-Beta zeolites with Si/Hf < 250 (Figure S4, SI), did not affect the trends observed here suggesting that oligomeric HfO_x species are inactive (compared to open Hf sites) for MPVO catalysis under the conditions studied here. As a result, we conclude that the active sites for MPVO catalysis on Hf-Beta are the open Hf sites titrated by CD_3CN with a vibrational frequency of ν(C≡N): 2313 cm^{-1} [38], consistent with prior observations made on Sn-containing zeolites [27,32,49].

3.6. Effect of framework polarity on MPVO catalysis over Hf-Beta zeolites

Measured initial MPVO rates (0.1 M cyclohexanone in 2-butanol, 373 K) were ~ 25x higher on hydrophobic Hf-Beta-F than on hydrophilic Hf-Beta-OH zeolites and apparent MPVO first-order rate constants (2-butanol solvent, 373 K) were ~ 6x higher on Hf-Beta-F than on Hf-Beta-OH zeolites despite normalization of cyclohexanol formation rates by the total number of open Hf sites determined from IR spectra of adsorbed CD_3CN (Fig. 11a). This difference in MPVO rate constants between hydrophobic and hydrophilic Hf-Beta zeolites is similar in magnitude to that observed on other M−Beta zeolites (where M = Sn, Ti, Zr) for both intra [32,36] and intermolecular [47,49,69] MPVO reactions in hydrogen-bonding solvents (e.g., water, alcohols).

These results are consistent with differences in the total number of SiOH groups counted by CD_3CN (Table 2) and IR spectra (Figure S42, SI) of 2-butanol adsorbed on Hf-Beta zeolites synthesized via direct crystallization in fluoride containing media (Hf-Beta-F (100)) and those prepared by grafting Hf sites into vacancy defects in dealuminated Beta zeolites (Hf-Beta-OH(109)) [47,49]. Consistent with observations on Sn-Beta-F zeolites [49], vibrational modes characteristic of monomeric (3615 cm^{-1}) and dimeric

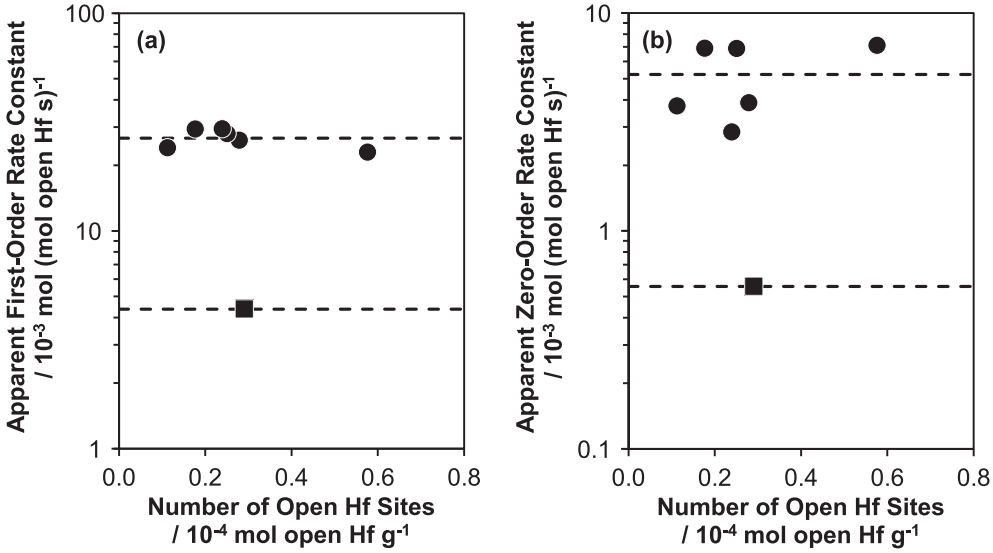

Fig. 11. Apparent MPVO (a) first-order and (b) zero-order rate constants (per open Hf, 373 K) measured on Hf-Beta-F samples (circles) and Hf-Beta-OH (square) in a 2-butanol solvent. Dashed lines represent the average of each data set.

(3510 cm^{-1}) 2-butanol species are observed on Hf-Beta-F(100) even up to saturation equilibrium pressures of 2-butanol. The presence of extended hydrogen-bonding networks (3100–3400 cm^{-1}) show larger peak intensities on Hf-Beta-F(100) than previously observed for Sn-Beta-F(302) zeolites [49], indicating that framework heteroatom content likely plays a role in stabilizing hydrogen-bonded solvent structures in confined spaces [60,77–80]. IR spectra of 2-butanol adsorbed on hydrophilic Hf-Beta-OH (109) are dominated by the presence of 2-butanol monomers (3600 cm^{-1}) and perturbed OH groups and extended hydrogen-bonded solvent structures (3100–3400 cm^{-1}), consistent with previous observations on Sn-Beta-OH where the presence of polar binding sites enables confined alcohols to adopt a liquid-like solvent structure [49]. These results indicate that the ability of the zeolite framework to regulate the structure of confined solvent networks extends beyond active site identity and depends on the polarity of the surround pore environment, which can be influenced by the altering the density of hydrophilic binding sites (e.g., SiOH defects, framework heteroatoms).

4. Conclusion

Lewis acid site counts were first validated by measuring IMECs on Sn-Beta zeolites using pyridine and CD_3CN titrants in order to benchmark site counts using established literature precedent. IMECs of CD_3CN bound to open and closed Sn sites were ~ 1.8x larger than those previously reported by Harris et al. [32], but gave total Lewis acid site counts that agreed with those measured by pyridine on six different Sn-Beta zeolites. These CD_3CN site counts were further validated by corroborating that apparent MPVO rate constants correlated with the total number of open Sn sites in agreement with prior reports [27,32,49].

Next, these validated experimental protocols were used to identify and quantify distinct active sites in Hf-Beta zeolites. While IR spectra of adsorbed CD_3CN showed the presence of two distinct Lewis acid sites, consistent with the presence of open (ν(C≡N): 2313 cm^{-1}) and closed (ν(C≡N): 2307 cm^{-1}) framework Hf sites [38], future work must aim to understand how Hf atoms position within the channels, intersections, and grain boundaries of the Beta framework. If the spectral features for Hf-Beta zeolites in this study correlate to similar features observed in Sn-Beta zeolites, the lower open/closed ratios for Hf-Beta would suggest that Hf is less stable in a defect-open configuration than Sn. Moreover, positioning the Lewis acid sites in predetermined positions within the framework of a zeolite would offer a powerful handle to modify catalytic activity.

IMECs for IR peaks reflecting pyridine bound to Lewis acidic Hf sites and CD_3CN bound to open and closed Hf sites gave similar counts for the total number of Lewis acid sites on Hf-Beta samples with different Si/Hf ratios. Notably, apparent first- and zero-order MPVO rate constants normalized per total Hf correlated with the number of open Hf sites, but not with the total number of closed Hf sites or total Lewis acid site counts. These data provide quantitative evidence that open Hf sites are the active sites for the MPVO reaction between cyclohexanone and 2-butanol, consistent with observations on Sn-Beta zeolites [27,32]. Measured initial MPVO rates were ~ 25× higher on hydrophobic Hf-Beta-F than on hydrophilic Hf-Beta-OH zeolites and apparent MPVO first-order rate constants were ~ 6× higher on Hf-Beta-F than on Hf-Beta-OH zeolites, after normalization of rates by the total number of open Hf sites, indicating that the catalytic consequences of confined solvent structures extend beyond the identity of the framework heteroatom. Collectively, the methods presented here for the quantification of Lewis acidic Hf sites in Hf-Beta zeolites provide a quantitative method for the normalization of catalytic turnover rates in order to decouple the effects of active site identity, solvation, and pore topology effects that convolute mechanistic interpretation of turnover rate differences measured on Lewis acidic zeolites used for the liquid-phase catalysis of oxygenates.

5. Personal acknowledgement

This article is dedicated to Prof. Michel Boudart, for his contributions to the conceptual, quantitative, and molecular understanding of fundamental catalytic chemistry; his legacy will be difficult to replicate, but we are inspired by his leadership and scientific merit.

Declaration of Competing Interest

The authors declare that they have no known competing financial interests or personal relationships that could have appeared to influence the work reported in this paper.

Acknowledgements

The authors thank the U.S. Department of Energy, Office of Basic Energy Sciences under Award DE-SC0016214 for support.

Appendix A. Supplementary material

Supplementary data to this article can be found online at https://doi.org/10.1016/j.jcat.2021.10.026.

References

[1] M. Boudart, A. Aldag, J.E. Benson, N.A. Dougharty, C. Girvin Harkins, On the specific activity of platinum catalysts, J. Catal. 6 (1) (1966) 92–99.
[2] M. Boudart, Turnover Rates in Heterogeneous Catalysis, Chem. Rev. 95 (3) (1995) 661–666.
[3] J.A. Dumesic, G.W. Huber, M. Boudart, Rates of catalytic reactions, Handbook of Heterogeneous Catalysis, 2nd ed.,., Wiley-VCH:, Weinheim, 2008.
[4] J.E. Benson, M. Boudart, Hydrogen-oxygen titration method for the measurement of supported platinum surface areas, J. Catal. 4 (1965) 704–710.
[5] G. Boreskov, A. Karnaukhov, Adsorption method for measuring the value of the platinum surface in platinized silica gels, Zh. Fiz. Khim. 26 (1952) 1814–1823.
[6] T.A. Dorling, R.L. Moss, The structure and activity of supported metal catalysts: I. Crystallite size and specific activity for benzene hydrogenation of platinum/silica catalysts, J. Catal. 5 (1966) 111–115.
[7] L. Spenadel, M. Boudart, Dispersion of Platinum on Supported Catalysts, J. Phys. Chem. 64 (1960) 204–207.
[8] H.S. Taylor, R.M. Burns, The Adsorption of Gases by Metallic Catalysts, J. Am. Chem. Soc. 43 (1921) 1273–1287.
[9] J.A. Dumesic, H. Topsøe, S. Khammouma, M. Boudart, Surface, catalytic and magnetic properties of small iron particles: II. Structure sensitivity of ammonia synthesis, J. Catal. 37 (1975) 503–512.
[10] J.A. Dumesic, H. Topsøe, M. Boudart, Surface, catalytic and magnetic properties of small iron particles: III. Nitrogen induced surface reconstruction, J. Catal. 37 (1975) 513–522.
[11] M. Boudart, Catalysis by Supported Metals, in, Adv. Catal., Academic Press (1969) 153–166.
[12] N.D. Spencer, R.C. Schoonmaker, G.A. Somorjai, Iron single crystals as ammonia synthesis catalysts: Effect of surface structure on catalyst activity, J. Catal. 74 (1982) 129–135.
[13] D.R. Kahn, E.E. Petersen, G.A. Somorjai, The hydrogenolysis of cyclopropane on a platinum stepped single crystal at atmospheric pressure, J. Catal. 34 (1974) 294–306.
[14] M. Boudart, Heterogeneous catalysis by metals, J. Mol. Catal. 30 (1985) 27–38.
[15] M. Boudart, A. Delbouille, J.A. Dumesic, S. Khammouma, H. Topsøe, Surface, catalytic and magnetic properties of small iron particles: I. Preparation and characterization of samples, J. Catal. 37 (1975) 486–502.
[16] J.H. Sinfelt, Hydrogenolysis of Ethane over Supported Platinum, J. Phys. Chem. 68 (1964) 344–346.
[17] D.E. Resasco, G.L. Haller, A model of metal-oxide support interaction for Rh on TiO_2, J. Catal. 82 (1983) 279–288.
[18] S.J. Tauster, Strong metal-support interactions, Acc. Chem. Res. 20 (1987) 389–394.
[19] S.J. Tauster, S.C. Fung, R.L. Garten, Strong metal-support interactions. Group 8 noble metals supported on titanium dioxide, J. Am. Chem. Soc. 100 (1978) 170–175.

[20] R.J. Madon, M. Boudart, Experimental Criterion for the Absence of Artifacts in the Measurement of Rates of Heterogeneous Catalytic Reactions, Ind. Eng. Chem. Fund. 21 (1982) 438–447.
[21] R.J. Madon, J.P. O'Connell, M. Boudart, Catalytic hydrogenation of cyclohexene: Part II, Liquid phase reaction on supported platinum in a gradientless slurry reactor, AIChE J. 24 (5) (1978) 904–911.
[22] J.W. Harris, J.S. Bates, B.C. Bukowski, J. Greeley, R. Gounder, Opportunities in Catalysis over Metal-Zeotypes Enabled by Descriptions of Active Centers Beyond Their Binding Site, ACS Catal. 10 (16) (2020) 9476–9495.
[23] J.S. Bates, B.C. Bukowski, J.W. Harris, J. Greeley, R. Gounder, Distinct Catalytic Reactivity of Sn Substituted in Framework Locations and at Defect Grain Boundaries in Sn-Zeolites, ACS Catal. 9 (7) (2019) 6146–6168.
[24] A. Rodríguez-Fernández, J.R. Di Iorio, C. Paris, M. Boronat, A. Corma, Y. Román-Leshkov, M. Moliner, Selective active site placement in Lewis acid zeolites and implications for catalysis of oxygenated compounds, Chem. Sci. 11 (37) (2020) 10225–10235.
[25] P.A. Wright, W. Zhou, J. Pérez-Pariente, M. Arranz, Direct Observation of Growth Defects in Zeolite Beta, J. Am. Chem. Soc. 127 (2) (2005) 494–495.
[26] H.Y. Luo, J.D. Lewis, Y. Román-Leshkov, Lewis Acid Zeolites for Biomass Conversion: Perspectives and Challenges on Reactivity, Synthesis, and Stability, Annu. Rev. Chem. Biomol. Eng. 7 (1) (2016) 663–692.
[27] M. BORONAT, P. CONCEPCION, A. CORMA, M. RENZ, S. VALENCIA, Determination of the catalytically active oxidation Lewis acid sites in Sn-beta zeolites, and their optimisation by the combination of theoretical and experimental studies, J. Catal. 234 (1) (2005) 111–118.
[28] R. Bermejo-Deval, R.S. Assary, E. Nikolla, M. Moliner, Y. Roman-Leshkov, S.-J. Hwang, A. Palsdottir, D. Silverman, R.F. Lobo, L.A. Curtiss, M.E. Davis, Metalloenzyme-like catalyzed isomerizations of sugars by Lewis acid zeolites, Proc. Natl. Acad. Sci. U. S. A. 109 (25) (2012) 9727–9732.
[29] R. Bermejo-Deval, M. Orazov, R. Gounder, S.-J. Hwang, M.E. Davis, Active Sites in Sn-Beta for Glucose Isomerization to Fructose and Epimerization to Mannose, ACS Catal. 4 (7) (2014) 2288–2297.
[30] J.D. Lewis, M. Ha, H. Luo, A. Faucher, V.K. Michaelis, Y. Román-Leshkov, Distinguishing Active Site Identity in Sn-Beta Zeolites Using 31P MAS NMR of Adsorbed Trimethylphosphine Oxide, ACS Catal. 8 (4) (2018) 3076–3086.
[31] P. Wolf, M. Valla, F. Núñez-Zarur, A. Comas-Vives, A.J. Rossini, C. Firth, H. Kallas, A. Lesage, L. Emsley, C. Copéret, I. Hermans, Correlating Synthetic Methods, Morphology, Atomic-Level Structure, and Catalytic Activity of Sn-β Catalysts, ACS Catal. 6 (7) (2016) 4047–4063.
[32] J.W. Harris, M.J. Cordon, J.R. Di Iorio, J.C. Vega-Vila, F.H. Ribeiro, R. Gounder, Titration and quantification of open and closed Lewis acid sites in Sn-Beta zeolites that catalyze glucose isomerization, J. Catal. 335 (2016) 141–154.
[33] J.W. Harris, W.-C. Liao, J.R. Di Iorio, A.M. Henry, T.-C. Ong, A. Comas-Vives, C. Copéret, R. Gounder, Molecular Structure and Confining Environment of Sn Sites in Single-Site Chabazite Zeolites, Chem. Mater. 29 (20) (2017) 8824–8837.
[34] Y.G. Kolyagin, A.V. Yakimov, S. Tolborg, P.N.R. Vennestrøm, I.I. Ivanova, Ivanova, II, Direct Observation of Tin in Different T-Sites of Sn-BEA by One- and Two-Dimensional ^{119}Sn MAS NMR Spectroscopy, J. Phys. Chem. Lett. 9 (13) (2018) 3738–3743.
[35] P. Ferrini, J. Dijkmans, R. De Clercq, S. Van de Vyver, M. Dusselier, P.A. Jacobs, B. F. Sels, Lewis acid catalysis on single site Sn centers incorporated into silica hosts, Coord. Chem. Rev. 343 (2017) 220–255.
[36] M.J. Cordon, J.W. Harris, J.C. Vega-Vila, J.S. Bates, S. Kaur, M. Gupta, M.E. Witzke, E.C. Wegener, J.T. Miller, D.W. Flaherty, D.D. Hibbitts, R. Gounder, Dominant Role of Entropy in Stabilizing Sugar Isomerization Transition States within Hydrophobic Zeolite Pores, J. Am. Chem. Soc. 140 (43) (2018) 14244–14266.
[37] J.D. Lewis, S. Van de Vyver, A.J. Crisci, W.R. Gunther, V.K. Michaelis, R.G. Griffin, Y. Román-Leshkov, A continuous flow strategy for the coupled transfer hydrogenation and etherification of 5-(hydroxymethyl)furfural using Lewis acid zeolites, ChemSusChem 7 (8) (2014) 2255–2265.
[38] S. Rojas-Buzo, P. Concepción, A. Corma, M. Moliner, M. Boronat, In-Situ-Generated Active Hf-hydride in Zeolites for the Tandem N-Alkylation of Amines with Benzyl Alcohol, ACS Catal. 11 (13) (2021) 8049–8061.
[39] Y. ZHU, G. CHUAH, S. JAENICKE, Selective Meerwein–Ponndorf–Verley reduction of α, βα, β-unsaturated aldehydes over Zr-zeolite beta, J. Catal. 241 (1) (2006) 25–33.
[40] Y. ZHU, G. CHUAH, S. JAENICKE, Chemo- and regioselective Meerwein–Ponndorf–Verley and Oppenauer reactions catalyzed by Al-free Zr-zeolite beta, J. Catal. 227 (1) (2004) 1–10.
[41] H.Y. Luo, D.F. Consoli, W.R. Gunther, Y. Román-Leshkov, Investigation of the reaction kinetics of isolated Lewis acid sites in Beta zeolites for the Meerwein–Ponndorf–Verley reduction of methyl levulinate to γ-valerolactone, J. Catal. 320 (2014) 198–207.
[42] Y. Wang, J.D. Lewis, Y. Román-Leshkov, Synthesis of Itaconic Acid Ester Analogues via Self-Aldol Condensation of Ethyl Pyruvate Catalyzed by Hafnium BEA Zeolites, ACS Catal. 6 (5) (2016) 2739–2744.
[43] M. Koehle, R.F. Lobo, Lewis acidic zeolite Beta catalyst for the Meerwein–Ponndorf–Verley reduction of furfural, Catal, Sci. Technol. 6 (9) (2016) 3018–3026.
[44] Y. Zhang, L. Qi, A. Lund, P. Lu, A.T. Bell, Mechanism and Kinetics of Acetone Conversion to Isobutene over Isolated Hf Sites Grafted to Silicalite-1 and SiO2, J. Am. Chem. Soc. 143 (22) (2021) 8352–8366.
[45] V.L. Sushkevich, D. Palagin, I.I. Ivanova, With Open Arms: Open Sites of ZrBEA Zeolite Facilitate Selective Synthesis of Butadiene from Ethanol, ACS Catal. 5 (8) (2015) 4833–4836.
[46] V.L. Sushkevich, A. Vimont, A. Travert, I.I. Ivanova, Spectroscopic Evidence for Open and Closed Lewis Acid Sites in ZrBEA Zeolites, J. Phys. Chem. C 119 (2015) 17633–17639.
[47] H. Zhang, Z.J. Quek, S. Jaenicke, G.-K. Chuah, Hydrophobicity and co-solvent effects on Meerwein-Ponndorf-Verley reduction/dehydration cascade reactions over Zr-zeolite catalysts, J. Catal. 400 (2021) 50–61.
[48] A. Corma, L.T. Nemeth, M. Renz, S. Valencia, Sn-zeolite beta as a heterogeneous chemoselective catalyst for Baeyer-Villiger oxidations, Nature 412 (2001) 423–425.
[49] J.R. Di Iorio, B.A. Johnson, Y. Roman-Leshkov, Ordered Hydrogen-Bonded Alcohol Networks Confined in Lewis Acid Zeolites Accelerate Transfer Hydrogenation Turnover Rates, J. Am. Chem. Soc. 142 (2020) 19379–19392.
[50] W.R. Gunther, V.K. Michaelis, R.G. Griffin, Y. Román-Leshkov, Interrogating the Lewis Acidity of Metal Sites in Beta Zeolites with ^{15}N Pyridine Adsorption Coupled with MAS NMR Spectroscopy, J. Phys. Chem. C 120 (2016) 28533–28544.
[51] J.C. Vega-Vila, J.W. Harris, R. Gounder, Controlled insertion of tin atoms into zeolite framework vacancies and consequences for glucose isomerization catalysis, J. Catal. 344 (2016) 108–120.
[52] C.A. Emeis, Determination of Integrated Molar Extinction Coefficients for Infrared Absorption Bands of Pyridine Adsorbed on Solid Acid Catalysts, J. Catal. 141 (2) (1993) 347–354.
[53] C. Morterra, G. Magnacca, A case study: surface chemistry and surface structure of catalytic aluminas, as studied by vibrational spectroscopy of adsorbed species, Catal. Today 27 (3-4) (1996) 497–532.
[54] E. PARRY, An Infrared Study of Pyridine Adsorbed on Acidic Solids. Characterization of Surface Acidity, J. Catal. 2 (5) (1963) 371–379.
[55] J. Datka, A.M. Turek, J.M. Jehng, I.E. Wachs, Acidic properties of supported niobium oxide catalysts: An infrared spectroscopy investigation, J. Catal. 135 (1992) 186–199.
[56] E. Selli, L. Forni, Comparison between the surface acidity of solid catalysts determined by TPD and FTIR analysis of pre-adsorbed pyridine, Microporous Mesoporous Mater. 31 (1-2) (1999) 129–140.
[57] B. Wichterlová, Z. Tvarůžková, Z. Sobalík, P. Sarv, Determination and properties of acid sites in H-ferrierite: A comparison of ferrierite and MFI structures, Microporous Mesoporous Mater. 24 (4-6) (1998) 223–233.
[58] S. Conrad, R. Verel, C. Hammond, P. Wolf, F. Göltl, I. Hermans, Silica-Grafted Sn^{IV} Catalysts in Hydrogen-Transfer Reactions, ChemCatChem 7 (20) (2015) 3270–3278.
[59] V.L. Sushkevich, I.I. Ivanova, A.V. Yakimov, Revisiting Acidity of SnBEA Catalysts by Combined Application of FTIR Spectroscopy of Different Probe Molecules, J. Phys. Chem. C 121 (21) (2017) 11437–11447.
[60] J.C. Vega-Vila, R. Gounder, Quantification of Intraporous Hydrophilic Binding Sites in Lewis Acid Zeolites and Consequences for Sugar Isomerization Catalysis, ACS Catal. 10 (20) (2020) 12197–12211.
[61] M. Miljković, B. Bird, M. Diem, Line shape distortion effects in infrared spectroscopy, Analyst 137 (17) (2012) 3954, https://doi.org/10.1039/c2an35582e.
[62] K. Rahmelow, Electronic influences on an infrared detector signal: nonlinearity and amplification Appl, Opt. 36 (10) (1997) 2123, https://doi.org/10.1364/AO.36.002123.
[63] K.S. Seshadri, R.N. Jones, The shapes and intensities of infrared absorption bands - A review, Spectrochim. Acta 19 (6) (1963) 1013–1085.
[64] K. Yamamoto, H. Ishida, Optical theory applied to infrared spectroscopy, Vib. Spectrosc 8 (1) (1994) 1–36.
[65] K.S. Seshadri, R.N. Jones, The shapes and intensities of infrared absorption bands—A review, Spectrochim. Acta 19 (6) (1963) 1013–1085.
[66] T. Bligaard, R.M. Bullock, C.T. Campbell, J.G. Chen, B.C. Gates, R.J. Gorte, C.W. Jones, W.D. Jones, J.R. Kitchin, S.L. Scott, Toward Benchmarking in Catalysis Science: Best Practices, Challenges, and Opportunities, ACS Catal. 6 (2016) 2590–2602.
[67] M. Boronat, A. Corma, M. Renz, Mechanism of the Meerwein-Ponndorf-Verley-Oppenauer (MPVO) Redox Equilibrium on Sn- and Zr-Beta Zeolite Catalysts, J. Phys. Chem. B 110 (2006) 21168–21174.
[68] V.A. Ivanov, J. Bachelier, F. Audry, J.C. Lavalley, Study of the Meerwein-Pondorff-Verley reaction between ethanol and acetone on various metal oxides, J. Mol. Catal. 91 (1994) 45–59.
[69] J. Wang, K. Okumura, S. Jaenicke, G.-K. Chuah, Post-synthesized zirconium-containing Beta zeolite in Meerwein–Ponndorf–Verley reduction: Pros and cons, Appl. Catal., A 493 (2015) 112–120.
[70] D.T. Bregante, A.M. Johnson, A.Y. Patel, E.Z. Ayla, M.J. Cordon, B.C. Bukowski, J. Greeley, R. Gounder, D.W. Flaherty, Cooperative Effects between Hydrophilic Pores and Solvents: Catalytic Consequences of Hydrogen Bonding on Alkene Epoxidation in Zeolites, J. Am. Chem. Soc. 141 (2019) 7302–7319.
[71] M. Boronat, A. Corma, M. Renz, P.M. Viruela, Predicting the activity of single isolated Lewis acid sites in solid catalysts, Chem. - Eur. J. 12 (2006) 7067–7077.
[72] L. Botti, S.A. Kondrat, R. Navar, D. Padovan, J.S. Martinez-Espin, S. Meier, C. Hammond, Solvent-Activated Hafnium-Containing Zeolites Enable Selective and Continuous Glucose-Fructose Isomerisation, Angew. Chem. Int. Ed. 59 (2020) 20017–20023.
[73] D.T. Bregante, D.W. Flaherty, Periodic Trends in Olefin Epoxidation over Group IV and V Framework-Substituted Zeolite Catalysts: A Kinetic and Spectroscopic Study, J. Am. Chem. Soc. 139 (20) (2017) 6888–6898.
[74] T. Iida, K. Ohara, Y. Román-Leshkov, T. Wakihara, Zeolites with isolated-framework and oligomeric-extraframework hafnium species characterized

with pair distribution function analysis, Phys. Chem. Chem. Phys. 20 (2018) 7914–7919.
[75] L. Botti, S. Meier, C. Hammond, Mechanistic Studies of Continuous Glucose Upgrading over Lewis Acidic Silicates by Operando UV–Vis and HSQC NMR, ACS Catal. 11 (2021) 1296–1308.
[76] J.D. Lewis, S. Van de Vyver, Y. Román-Leshkov, Acid-Base Pairs in Lewis Acidic Zeolites Promote Direct Aldol Reactions by Soft Enolization, Angew. Chem. Int. Ed. 54 (2015) 9835–9838.
[77] B.C. Bukowski, J.S. Bates, R. Gounder, J. Greeley, Defect-Mediated Ordering of Condensed Water Structures in Microporous Zeolites, Angew. Chem. Int. Ed. 58 (2019) 16422–16426.
[78] J.S. Bates, R. Gounder, Kinetic effects of molecular clustering and solvation by extended networks in zeolite acid catalysis, Chem. Sci. 12 (2021) 4699–4708.
[79] S. Eckstein, P.H. Hintermeier, M.V. Olarte, Y. Liu, E. Baráth, J.A. Lercher, Elementary steps and reaction pathways in the aqueous phase alkylation of phenol with ethanol, J. Catal. 352 (2017) 329–336.
[80] J.S. Bates, B.C. Bukowski, J. Greeley, R. Gounder, Structure and solvation of confined water and water-ethanol clusters within microporous Bronsted acids and their effects on ethanol dehydration catalysis, Chem. Sci. 11 (2020) 7102–7122.